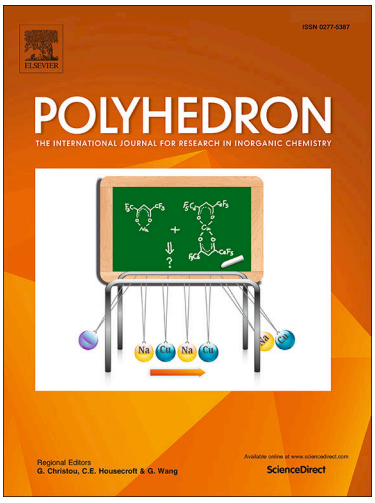

Synthesis and Crystal Structures of Zinc(II) coordination polymers of trimethylenedipyridine (tmdp), 4-nitrobenzoic (Hnba) and 4-biphenylcarboxylic acid (Hbiphen) for adsorptive removal of methyl orange from aqueous solution

Adedibu C. Tella, Adetola C. Oladipo, Vincent O. Adimula, Victoria T. Olayemi, Tendai O. Dembaremba, Adeniyi S. Ogunlaja, Guy J. Clarkson, Richard I. Walton

PII: S0277-5387(20)30476-9
DOI: https://doi.org/10.1016/j.poly.2020.114819
Reference: POLY 114819

To appear in: *Polyhedron*

Received Date: 13 August 2020
Revised Date: 17 September 2020
Accepted Date: 28 September 2020

Please cite this article as: A.C. Tella, A.C. Oladipo, V.O. Adimula, V.T. Olayemi, T.O. Dembaremba, A.S. Ogunlaja, G.J. Clarkson, R.I. Walton, Synthesis and Crystal Structures of Zinc(II) coordination polymers of trimethylenedipyridine (tmdp), 4-nitrobenzoic (Hnba) and 4-biphenylcarboxylic acid (Hbiphen) for adsorptive removal of methyl orange from aqueous solution, *Polyhedron* (2020), doi: https://doi.org/10.1016/j.poly.2020.114819

Synthesis and Crystal Structures of Zinc(II) coordination polymers of trimethylenedipyridine (tmdp), 4-nitrobenzoic (Hnba) and 4-biphenylcarboxylic acid (Hbiphen) for adsorptive removal of methyl orange from aqueous solution

Adedibu C. Tella[a], Adetola C. Oladipo[a,b], Vincent O. Adimula[a], Victoria T. Olayemi[a,c], Tendai O. Dembaremba[d], Adeniyi S. Ogunlaja[d], Guy J. Clarkson[e] and Richard I. Walton[e]

[a]Department of Chemistry, P.M.B.1515, University of Ilorin, Ilorin, Kwara State, Nigeria

[b]Department of Physical Sciences, Industrial Chemistry Programme, Landmark University, P.M.B.1001, Omu-Aran, Kwara State, Nigeria.

[c]Department of Chemistry, College of Pure and Applied Sciences, Kwara State University, P.M. B 1530, Malete, Nigeria.

[d] Department of Chemistry, Nelson Mandela University, P.O. Box 77000, Port Elizabeth, 6031, South Africa.

[e]Department of Chemistry, University of Warwick, Coventry, CV4 7AL, UK

Abstract

Two novel Zn(II) coordination polymers (CPs), $[Zn(nba)_2(tmdp)]_n$ (**1**) and $[Zn(biphen)_2(tmdp)]_n$ (**2**), were synthesised by reacting $Zn(NO_3)_2{\cdot}6H_2O$ and 4,4'-trimethylenedipyridine (tmdp) with corresponding carboxylates: 4-nitrobenzoic (Hnba) and 4-biphenylcarboxylic acid (Hbiphen). Their structures were characterized by elemental analysis, IR spectroscopy, thermogravimetric analysis (TGA), powder X-ray diffraction (PXRD) and single-crystal X-ray diffraction. Compounds **1** and **2** are one-dimensional CPs with the zinc(II) carboxylate units bridged through the N-donor spacer ligand. The zinc (II) atom adopts a tetrahedral arrangement in **1** and **2** coordinated by two nitrogen atoms from two tmdp ligand molecules and two deprotonated oxygen atoms from two carboxylate ligand molecules. The adsorption capacities of MO in this study was found to be 546.31 mg/g and 22.67 mg/g for **1** and **2**, respectively. DFT studies confirmed that adsorption is primarily due to π-π stacking and electrostatic interactions between MO and **1**. It is noteworthy that binding energy (BE) values for **1** (-74.14 KJ/mol) and **2** (-61.11 KJ/mol) correlate reasonably well with the observed adsorption capacities of MO. The study demonstrated that **1** has higher adsorption efficiency in comparison to **2** and could be an effective and easily reusable adsorbent for the removal of MO from wastewater.

Keywords: Coordination polymer; X-ray Crystallography; Adsorption ; Methyl orange; DFT.

l. Introduction

Coordination polymers (CPs) are a class of functional materials comprising metal ions bridged by organic linkers [1]. They are able to form 1D, 2D and 3D architectures and they possess great potential in numerous applications such as gas adsorption, catalysis, drug delivery, luminescence and environmental remediation [2–5]. The organic linkers provide good flexibility and improves functionality of the CPs. 4-nitrobenzoic (Hnba) is a monotopic linker, 4-biphenylcarboxylic acid (Hbiphen) is a bridging ligand and acts as a proton donor while 4,4'-trimethylenedipyridine (tmdp) is an N-donor ditopic ligand [6]. On the other hand, the common binding sites observed for Zn(II) ions coordination polymers are 4-, 5- to 6-coordinate [7].

Organic compounds present in wastewater effluents, released to the environment due to industrial or agricultural activities have detrimental effects on public health [8]. Dyes are the largest contributor of organic pollutants. They exhibit toxicity even when present in low concentrations. They have mutagenic and carcinogenic effects and can also cause respiratory problems [9]. Due to their industrial applications, dyes are found in effluents from pharmaceutical, pulp and paper, paint, and some other industries. About one fifth of all the dyes produced worldwide gets discharged into waterbodies through the effluents from textile industries [10].The most abundant compounds (60 – 70 %) in textile waste are azo dyes [11]. Methyl orange (MO) is one of the azo dyes that are often used as textile dyes and have different structure which depends on the acidity (Figure S1). Non-biodegradable methyl orange can produce several environmental pollution problems by releasing toxic and carcinogenic compounds in the waters even at low concentrations and results in induced lesions and cancers [12]. Hence, the need to effectively remove MO from the water bodies.

Methods which have been used to clean up wastewaters that are polluted with non-biodegradable compounds include photocatalysis, membrane filtration and adsorption [13–17]. Adsorption presents the simplest, most economical and efficient way of remediation [18]. Conventional adsorbents such as mesoporous carbon [19], chitosan composites [20], montmorillonites [21] etc. were employed for the removal of MO dye from water but they suffer from drawbacks such as lack of property tunability and poor selectivity. Considering

the increasing rate of pollution, the development of more effective materials that exhibit high selectivity and adsorption capacities is paramount.

In this regard, the attention of researchers has been attracted to the coordination polymers which consist of metal ions or nodes and bridging organic ligands, suitable materials for a diverse range of applications especially in adsorption, separation and purification [22–24].

Compared to conventional adsorbents, CPs have proven to be effective in adsorption based on distinct properties they display which include large pores, surface area, high tunability. These distinct properties make coordination polymers a leading edge over other adsorbents.

However, the interaction of active functional groups present on the adsorbents and the adsorbate molecules, through other mechanisms such as hydrogen bonding, electrostatic interaction, pie-pie interaction etc., could contribute more to the efficiency of adsorbents [25, 26]. Studies have shown that MOFs are effective in removing dyes *via* electrostatic interaction [27, 28]. Fe-terephthalate (MOF-235) presented adsorption capacities of 477 and 187 mg /g, for MO and methylene blue (MB), respectively [27]. Similarly, coordination polymers have proven effective in adsorption applications despite their limited voids and surface areas [29–32].

We previously communicated the adsorption of fluorescein and methyl orange dyes, pyrene, ciprofloxacin and the adsorptive desulphurization of organosulfur in fuel using CPs [33–38]. In this report, two new Zn(II) CPs, $[Zn(nba)_2(tmdp)]_n$ (**1**) and $[Zn(biphen)_2(tmdp)]_n$, (**2**) were synthesized and employed for the removal of MO from aqueous solution. In addition, DFT study was carried out to investigate specific interactions that aided the removal of MO dye. Compound **1** was found to be more effective for the adsorptive uptake of MO dye.

2. Experimental

2.1 Materials

$Zn(NO_3)_2{\cdot}6H_2O$ (98%), 4-nitrobenzoic acid (98%), 4-biphenylcarboxylic acid (99%), 4,4'-trimethylenedipyridine (98%), dimethylformamide (DMF, 99%), triethylamine (99.5%), hydrochloric acid (37%), ethanol (99.9%), sodium hydroxide pellets (97%), and methyl orange dye were procured from Sigma-Aldrich, Germany and used as supplied.

2.2 Synthesis

Synthesis of $[Zn(nba)_2(tmdp)]_n$ (1): $Zn(NO_3)_2{\cdot}6H_2O$ (0.296 g, 1 mmol), 4-nitrobenzoic acid (Hnba) (0.167 g, 1 mmol) and 4,4-trimethylenedipyridine (0.199 g, 1 mmol) (tmdp) were added to 15 mL DMF, followed by adding 3 drops of triethylamine (for deprotonation). The

solution was stirred for 2 hours at RT (~27°C) and resulted into a clear colourless solution. Block-shaped crystals obtained after 7 days were separated out by filtration and dried at room temperature in a dessicator. (**Scheme S1**). M. wt: 595 g/mol; Melting point: 240°C; Yield: 78%, Anal. calc. for $C_{27}H_{22}N_4O_8Zn$: C, 54.37; H, 3.69; N, 9.40; Found: C, 53.69; H, 3.62; N, 9.13; IR KBr pellets (cm^{-1}) 3031 (br), 2923 (w), 1651(s), 1575 (w), 1448 (m), 1338(s), 1222 (w), 632 (m), 437 (w).

Synthesis of $[Zn(biphen)_2(tmdp)]_n$ (2): $Zn(NO_3)_2 \cdot 6H_2O$ (0.296 g, 1 mmol), 4-biphenylcarboxylic acid (Hbiphen) (0.296 g, 1 mmol) and 4,4-trimethylenedipyridine (0.199 g, 1 mmol) (tmdp) were added to 15 mL DMF, followed by adding 3 drops of triethylamine (for deprotonation). The solution was stirred for 2 hours at RT (~27°C) and resulted into a clear colourless solution. Block-shaped crystals obtained after 23 days were separated out by filtration and dried at room temperature in a dessicator (**Scheme S1**) M. wt: 658 g/mol; Melting point: 260 ^oC; Yield: 81%, Anal. calc. for $C_{39}H_{32}N_2O_4Zn$: C, 71.12; H, 4.86; N, 4.25; Found: C, 70.05; H, 4.95; N, 4.14; IR KBr pellets ($cm^{-1)}$ 3031(br), 2825(w), 1602 (s), 1543(w), 1431 (m), 1349 (s), 1185 (w), 682 (w), 455 (w).

2.3 Instrumentation

Elemental analysis was done using a PerkinElmer PE-2400 CHN analyser. FT-IR measurements were carried out with a Shimadzu 8400 spectrophotometer (8400, Shimadzu, Japan). Powder X-ray diffraction (PXRD) patterns were collected using a Siemens D5000 diffractometer operating with Cu $K_{\alpha 1/2}$ radiation in flat-plate geometry. TGA/DSC analysis was carried out with a Mettler Toledo TGA/DSC 1-600 instrument with a heating rate of 10 °C min^{-1} from 25 °C to 1000 °C. Nitrogen adsorption measurements, from which the surface area and pore volume were obtained, were performed on Nova 4200e Quantachrome (USA). For X-ray crystallographic analysis, a single crystal was chosen and placed on a glass fibre with Fomblin oil and mounted on an Xcalibur Gemini diffractometer with a Ruby CCD area detector and kept at 150(2) K during data collection. Using Olex2 [39], the structure was solved with the ShelXT [40] structure solution program using intrinsic phasing and refined with the ShelXL [41] refinement package using Least Squares minimization.

2.4 Adsorption experiment

Batch adsorption studies were employed to optimize the adsorption of MO on $[Zn(nba)_2(tmdp)]_n$ (**1**) and $[Zn(biphen)_2(tmdp)]_n$ (**2**). This was carried out by agitating 50 mL

sample solutions in a 250 mL flask at 165 rpm for 120 min in an incubator shaker. Operational parameters namely pH, adsorbate initial concentration, time, adsorbent dosage and temperature, were optimized for the adsorption process on **1**. The effect of pH was studied within the pH range of 2 to 12 (using 0.1 M HCl and 0.1 M NaOH for acidic and basic pH ranges, respectively). Adsorbent dosage (0.01-0.05 g) in 50 mL of 500 mg/L MO solution was employed to study the effect of adsorbent mass at the optimum pH. Solution temperature effect was investigated within 298-333 K at the optimum pH and adsorbent dosage. Different concentrations in the range 20-500 ppm were made from the stock solution to study the initial concentration effect on adsorption using 0.02 g adsorbent dosage at the optimum pH. The effect of time was investigated within 30-480 min, at the optimum pH and concentration, temperature and adsorbent dosage.

To determine the amount of adsorbate remaining after adsorption, the adsorbents were removed from the supernatants by centrifuging at 1200 rpm for 20 min. The residual dye concentrations of the supernatant was analysed using a UV−Vis spectrophotometer by monitoring the absorbance at the λ_{max} of 467 nm. The amount (q_e) of adsorbate per gram of adsorbent was calculated using the equation:

$$q_e = \frac{(C_o - C_e)V}{W} \quad \ldots\ldots\ldots\ldots\ldots\ldots\ldots\ldots\ldots\ldots\ldots\ldots\ldots\ldots\ldots\ldots \; Equation\ 2.1$$

Where C_o = initial concentration of the adsorbate (mg/L), C_e = equilibrium concentration of the adsorbate (mg/L), V = adsorbate solution volume (L) and W = mass of adsorbent used (g).

The adsorption data was fitted into Langmuir, Freundlich, Temkin and Dubinin Radushkevich isotherm models; and pseudo-first order, pseudo-second order, intraparticle diffusion, Bangham and Boyd kinetic models.

2.5 Theoretical studies

Theoretical studies were carried out using Biovia Materials Studio 2018. The Forcite tool was applied for pre-optimization of geometry to ultra-fine quality and to determine the most plausible starting positions (structures with the lowest total energy) to model the interactions between adsorbents and adsorbates. Literature methods were slightly modified to carry out the DFT studies using the DMol^3 module on the Forcite pre-optimized structures with convergence threshold parameters set at default (medium); energy = 0.00002, gradient =

0.004 and displacement = 0.005 [42, 43]. The generalized gradient approximation (GGA) with Perdew-Burke-Ernzerhof (PBE) parametrization functional was applied with Grimme for DFT-D correction. Density functional semi-core pseudopotentials were fitted to all electrons with a double numerical plus (DNP) polarization basis set and a real-space orbital global cut-off of 4.4 Å. The studies were first carried out in gas phase before the conductor-like screening model (COSMO) was applied using water at a dielectric constant of 78.54. The binding energies between the adsorbents and adsorbates were then determined by subtracting the sum of the energies of the adsorbent and adsorbate from the total energy of the adsorbent/adsorbate dye cluster, i.e.

$$\Delta E\ (BE) = E_{\frac{adsorbent}{adsorbate}} - \mathrm{E}_{adsorbent} + \mathrm{E}_{adsorbate} \ldots\ldots\ldots\ldots\ldots\ldots\ldots\ldots\ldots\ldots Equation\ 2.2$$

3. Results and discussion

3.1 FT-IR

The FT-IR spectra of ligands, compounds **1** and **2** are shown in **Figure S2**. The broad band for -COOH around 2576-3096 cm^{-1} noticeable in the IR spectrum of both carboxylic acids disappeared in spectra **1** and **2** indicating deprotonation and coordination with metal ion. C=O bands of 1732 and 1716 cm^{-1} in Hnba and Hbiphen are also absent in **1** and **2,** respectively. The COO^- sym, asym stretching frequencies are at 1651, 1338 cm^{-1} (in **1**) and 1602, 1349 cm^{-1} (in **2**). The difference between these stretching frequencies [$\nu_{as}(COO^-)$–$\nu_s(COO^-)$] in **1** and **2** are 213 and 253 cm^{-1} respectively. This agrees with unidentate coordination of the carboxylate group [44]. The incorporation of co-ligand is supported by the additional bands that appear in the mid IR region. ν(C=N) band was located at 1585 cm^{-1} for the tmdp, shifted to 1575 cm^{-1} (in **1**) and 1543 cm^{-1} (in **2**) on coordinating with Zn(II) ion. The bands at 632- 682 cm^{-1} and 437 – 455 cm^{-1} indicate Zn-N and Zn-O stretching vibrations, respectively.

3.2 PXRD results

The simulated and as prepared (measured at room temperature) PXRD patterns of **1** and **2** are presented in **Figure 1a** and **1b**. The similarity of both patterns confirmed the purity of the bulk materials. The slight difference in relative peak intensities of **1** could be as a result of the preferred orientation: the well-shaped crystals aligned in one major direction; therefore, the

powder XRD pattern might not be a representative of all orientations, unlike the simulated pattern which includes diffraction from all crystal planes.

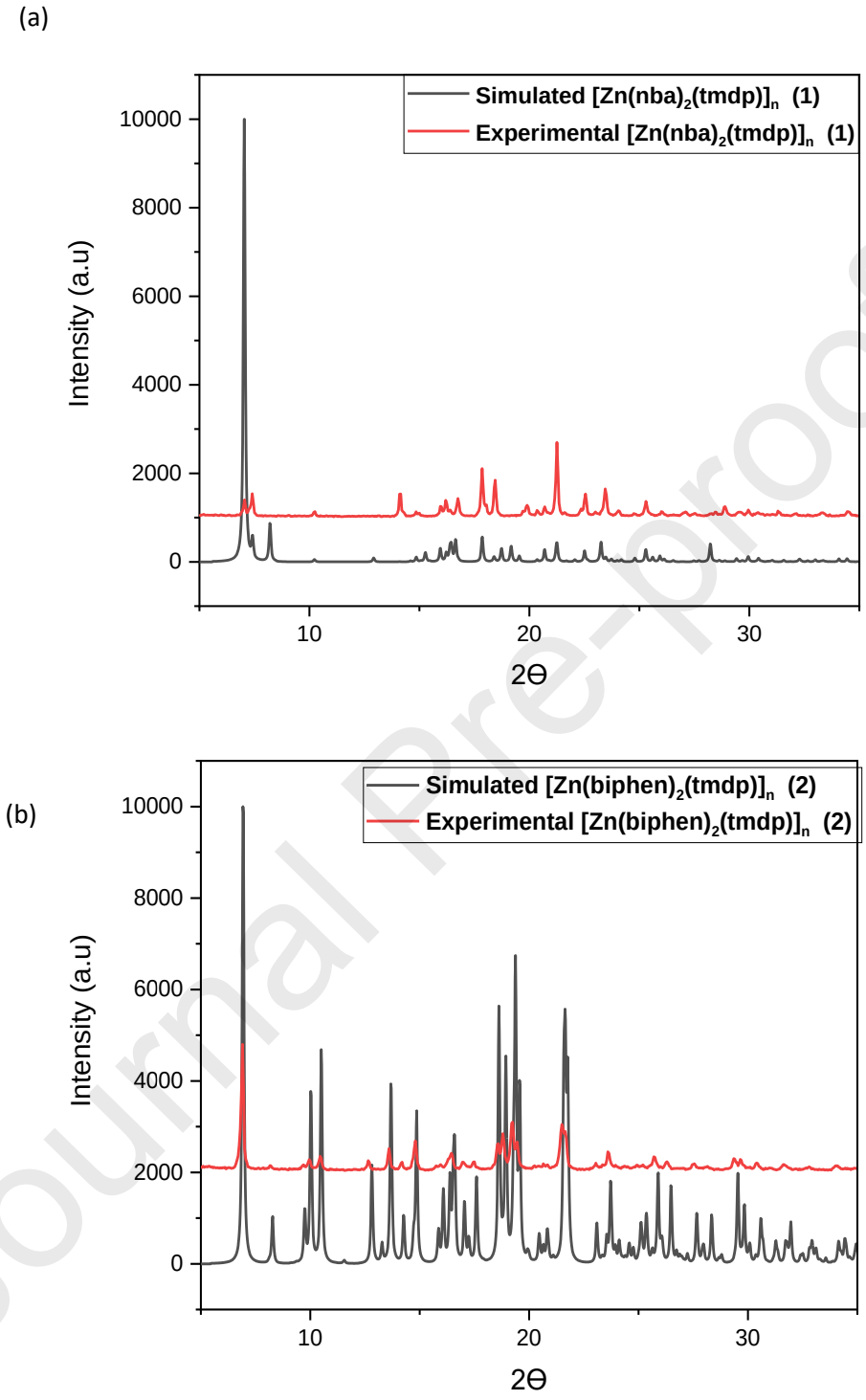

Figure 1: Simulated and as-prepared PXRD patterns of: (a) [Zn(nba)$_2$(tmdp)]n (**1**) (b) [Zn(biphen)$_2$(tmdp)]n (**2**).

3.3 X-ray crystallographic results

Crystal data and data collection summary for **1** and **2** are shown on **Table S1**. Bond distances and angles around the metal ion are shown in **Table 1**.

[Zn(nba)$_2$(tmdp)]n (1): The ORTEP diagram and the atom numbering scheme are shown in **Figure 2**. Compound **1** with Zn:nba:tmdp in a 1:2:2 mole ratio exhibited a unidentate mode of coordination of the two molecules of 4-nba ligand, and they adopted a trans-conformation. The zinc atom is coordinated by two deprotonated oxygen atom (O1 and O1) from two nba molecules and two pyridyl nitrogen atoms (N11 and N11) from two tmdp ligands. It crystallizes in the orthorhombic crystal system with centrosymmetric space group *P b c m*. Zn (II) is located on a two-fold axis. The asymmetric unit is composed of one Zn(II) ion, one molecule of nba and half molecule of tmdp ligand.

The observed Zn-O distance of 1.910 Å for the carboxylate oxygen atoms of both nba molecules indicates the same coordination strength of both to the Zn(II). These distance values and Zn - N distance of 2.071 Å, agree with reported values of Zn (II) CPs [45,46]. Bond angles around Zn (II) in **1** vary between 98.66 and 118.35^o, showing a distorted tetrahedral coordination sphere [ZnN_2O_2]. This deviation from regular tetrahedral was ascertained by calculating the parameters τ and τ' (τ = τ' = 0 for square planar, τ = τ'=1 for tetrahedral) [47,48]. The value obtained for both is 0.87, indicating that the tetrahedral geometry is distorted. Two adjacent Zn(II) atoms are connected by the tmdp ligand to form 1D CPs, with the two carboxylate ligand molecules acting as pendants as shown in **Figure S3**.The compound is packed in a way that leads to the proximity of the nba ligands of adjacent layers. The centroid to centroid distance of over 4 Å between the aromatic rings of neighbouring molecules indicates that there are no π-π stacking interactions in the compounds. A detailed structural analysis revealed that there are weak short contacts and C-H•••O intermolecular interactions of the CH_2 groups of nba and tmdp ligands with the COO^- and NO_2 oxygen atoms of the nba ligand as shown in **Figure S4.** Some of these contacts are N11…..O2 (3.069 Å), C5-H5….O9 (2.649 Å), C12-H12….O12 (2.641 Å) and C16-H16….O1 (2.538 Å). These contacts develop the adjacent 1D chains into 2D packing structure as shown in **Figure S5**.

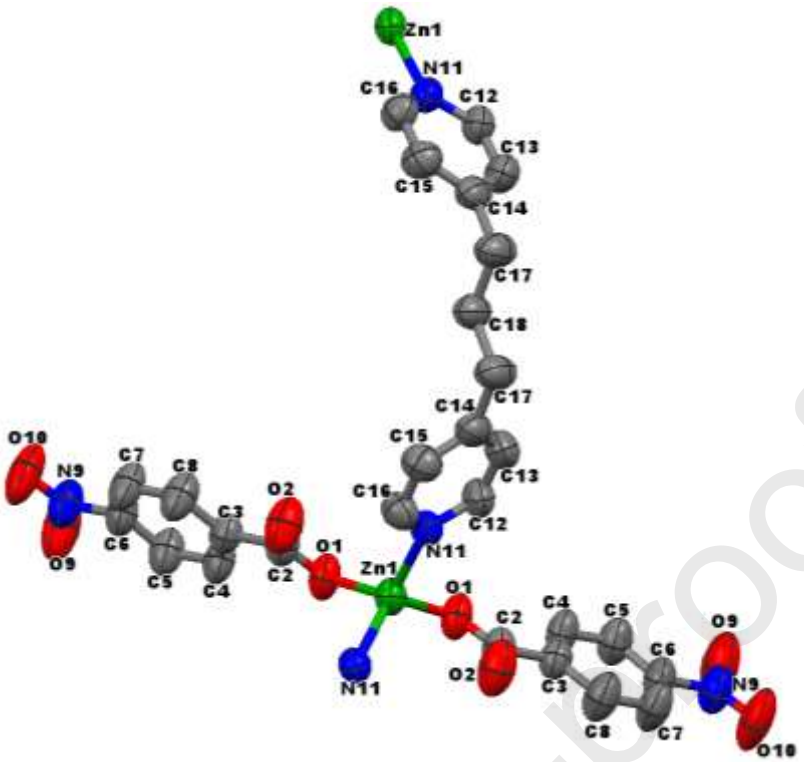

Figure 2: ORTEP diagram of [Zn(nba)$_2$(tmdp)]n (**1**) (Ellipsoids drawn at 50% probability level, hydrogen atoms omitted for clarity)

[Zn(biphen)$_2$(tmdp)]n (2): The zinc atom in **2** is coordinated in a monodentate mode by two deprotonated oxygen atoms (O1A and O1B) from two biphen molecules and two pyridyl nitrogen atoms (N17 and N27) from two tmdp molecules (**Figure 3**). The zinc atoms exhibit tetrahedral geometry, coordinated to two tmdp ligands and two biphen ligands in a trans-conformation. The parameters τ and τ' equal 0.86, this confirms a distorted tetrahedral geometry [48]. It crystallizes in the monoclinic crystal system (α = γ = 90°, β =105.9928) with space group *C2/c*. The asymmetric unit for compound **2** is composed of a zinc atom, two biphen molecules and a tmdp ligand. The Zn-O distances within 1.9501-1.9801 Å, and the Zn-N distances within 2.0392-2.0857 Å, compare well to reported values of existing Zn(II) MOFs [45,46]. The coordination strengths of the carboxylate oxygen atoms are close, judging from the small difference between the Zn-O bond length. This is also applicable to the coordinated pyridyl nitrogen atoms.

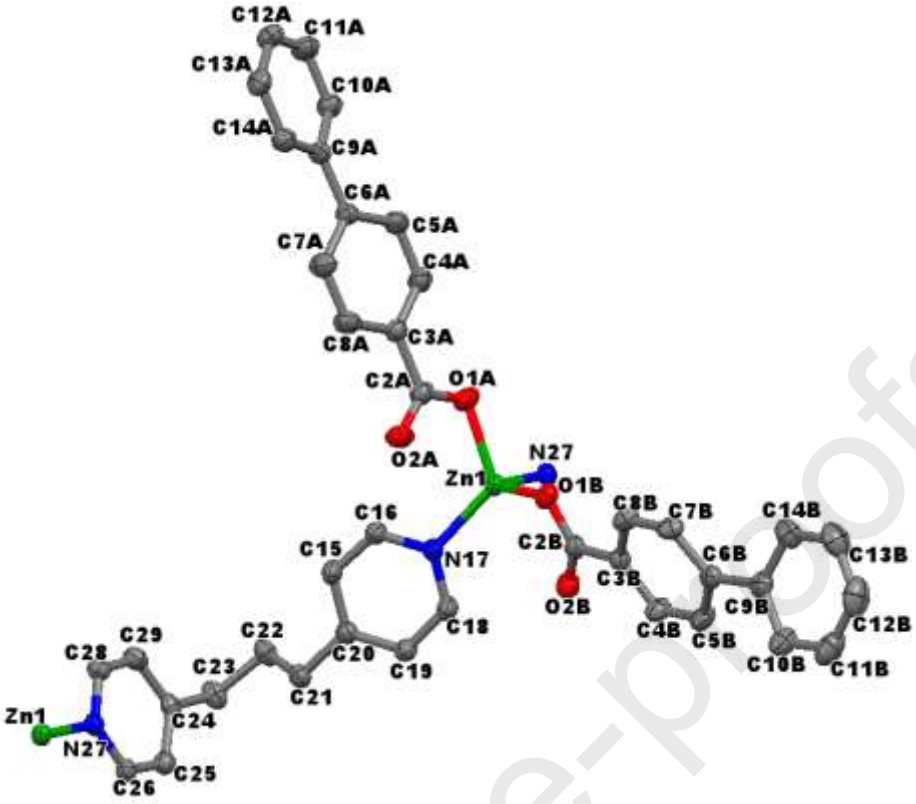

Figure 3. ORTEP diagram of [Zn(biphen)$_2$(tmdp)]n (**2**) (Ellipsoids drawn at 50% probability level, hydrogen atoms omitted for clarity)

Table 1. Bond lengths and angles around Zn(II) in **1** and **2**.

[Zn(nba)$_2$(tmdp)]n (1)				**[Zn(biphen)$_2$(tmdp)]n (2)**			
Bond length (Å)		**Bond angles (º)**		**Bond length (Å)**		**Bond angles (º)**	
Zn1-O1	1.9097	O1-Zn1-O11	106.48	Zn1-N17	2.0392	O1B-Zn1-O1A	108.10
Zn1-N11	2.0707	O1-Zn1-O1	98.66	Zn1-O1B	1.9501	O1B-Zn1-N17	120.53
		O1-Zn1-O11	118.35	Zn1-N27	2.0857	O1B-Zn1-N27	109.44
		N11-Zn1-O1	118.35	Zn1-O1A	1.9801	O1A-Zn1-N17	117.89
		N11-Zn1-N11	108.83			O1A-Zn1-N27	93.39
		O1-Zn1-N11	106.48			N17-Zn1-N27	103.51

The tmdp ligands link adjacent zinc atoms to give 1D chains, having two biphen molecules as pendants are shown in **Figure S6**, the Zn•••Zn distance being 11.476 Å. No hydrogen bonding interaction was found, but weak van der Waals interactions exist between O1A and N27 (**Figure S7**). The distance of 3.182 Å in between the two coordinated oxygen atoms, O1A and O1B is higher than the limit for O…O van der Waals interaction between them. The

packing diagram of **2** are presented in **Figure S8** and is stabilized, in addition to the covalent bonds, by the homo- interaction of benzene rings of adjacent biphen ligands from an adjacent chain, through π-π stacking, the centroid-centroid distance being within the limit of π-π interaction of the aromatic rings [49] whereas hetero-interaction between the pyridyl ring of the tmdp ligand and the phenyl ring of the biphen ligand is not possible due to a large centroid-centroid distance of 6.596 Å between them [50].

The methylene groups between the two pyridyl rings of tmdp ligand confer flexibility on it. The flexibility is confirmed by the significant dihedral angle (176^o for **1** and 174^o for **2**) between the planes of the two pyridyl rings. In **1**, the plane of the carboxylic group of the nba ligand is nearly coplanar with that of the aromatic ring, with a dihedral angle of 4.74^o in **1** and 0.64^o in **2** [51].

While porosity in higher dimensional CPs is as a result of the channels in their framework, porosity in 1D CPs depends on their packing [52,53]. For example, a 1D CP that is packed in a manner in which two adjacent linear chains hug each other led to a double stranded structure with less porosity compared to one with its adjacent chains parallel to each other [54]. Space filling representation of the packing view of the unit cells for **1** and **2** are shown in figures 4 and 5, this revealed the presence of voids within CPs.

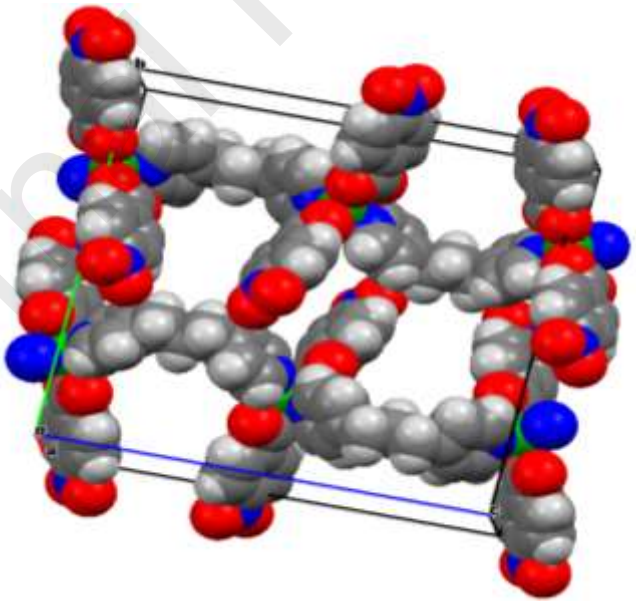

Figure 4. Space filling representation of the packing view of **1**.

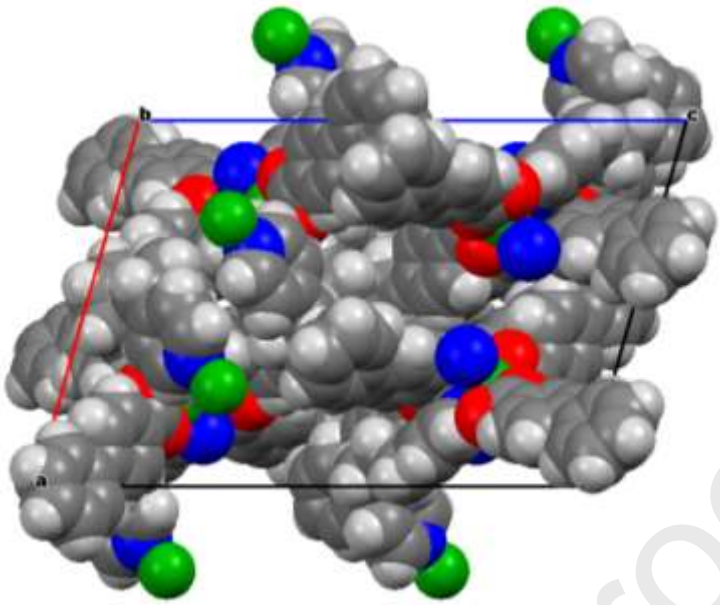

Figure 5: Space filling representation of the packing view of **2**.

3.4 BET Surface Area measurements

Specific surface area of [Zn(nba)$_2$(tmdp)]n **(1)** and [Zn(biphen)$_2$(tmdp)]n **(2)** are determined by multipoint Brunauer, Emmett and Teller (BET) method at relative pressure (P/P_o) from 0.04 to 0.32. BET surface area plots of **1** and **2** are presented in **Figure S9** and **S10,** respectively, and it demonstrated the typical linear characteristic plot with correlation coefficient of $r^2 \sim 0.99$. The BET surface area of [Zn(biphen)$_2$(tmdp)]n **(2)** (444.10 m^2/g) was reportedly lower than [Zn(nba)$_2$(tmdp)]n **(1)** (530.33 m^2/g). The slightly lower surface area of **2** was attributed to the structural difference between the two compound and the presence of 4-biphenylcarboxylic acid (Hbiphen) within the crystal lattice. This influences the pore diameter of [Zn(nba)$_2$(tmdp)]n **(1)** (3.04 nm) and [Zn(biphen)$_2$(tmdp)]n **(2)** (2.92 nm). High surface area is beneficial for improving adsorption dye materials.

3.5 Hirshfeld Surface Analyses

Hirshfeld surface analyses [55] showed intermolecular interactions such as O–H···O, O–H···N and C–H···π. Two sharp O–H spikes are typical O–H···O interaction and it comprised of 42.3 and 12.4% for [Zn(nba)$_2$(tmdp)]n **(1)** and [Zn(biphen)$_2$(tmdp)]n **(2)**, respectively.

Thus, indicating that compound (**1**) contributes a higher O–H···O interaction compared to (**2**).

The fingerprint plots showed that C–H contacts was highest on (**2**) (35.5%), and this is closely related to C–H···π interactions [37].The percentage of major contributions such as O-H, N-H, C-C, and C-H, interatomic contacts for each molecule are compiled in Table 1. Molecular Hirshfeld surface such as d_{norm}, shape index and curvedness confirming interactions between neighbouring molecules of [Zn(nba)$_2$(tmdp)]n **(1)** and [Zn(biphen)$_2$(tmdp)]n **(2)** are presented Figure 6. Fingerprint plot of [Zn(nba)$_2$(tmdp)]n **(1)** and [Zn(biphen)$_2$(tmdp)]n **(2)** in full and resolved into H···O, C···N, and H···N are presented Figures 7 and 8, respectively.

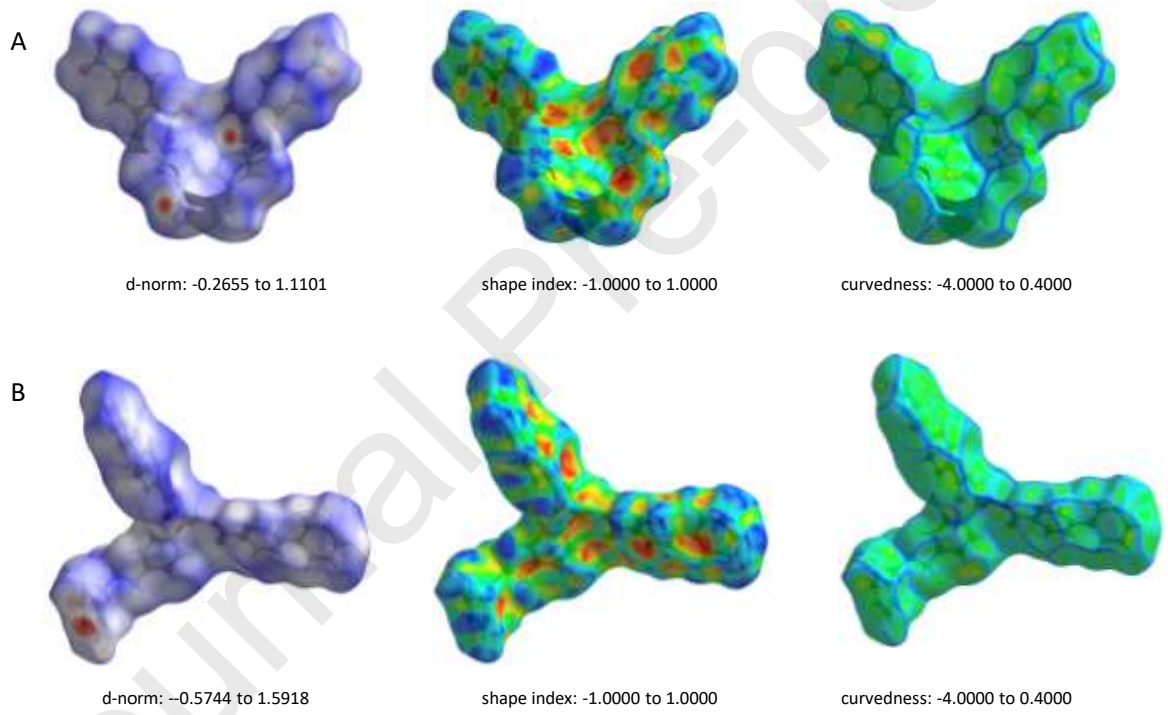

Figure 6: Molecular Hirshfeld surface such as d_{norm}, shape index and curvedness for (A) [Zn(nba)$_2$(tmdp)]$_n$ **(1)** and (B) [Zn(biphen)$_2$(tmdp)]$_n$ **(2)**

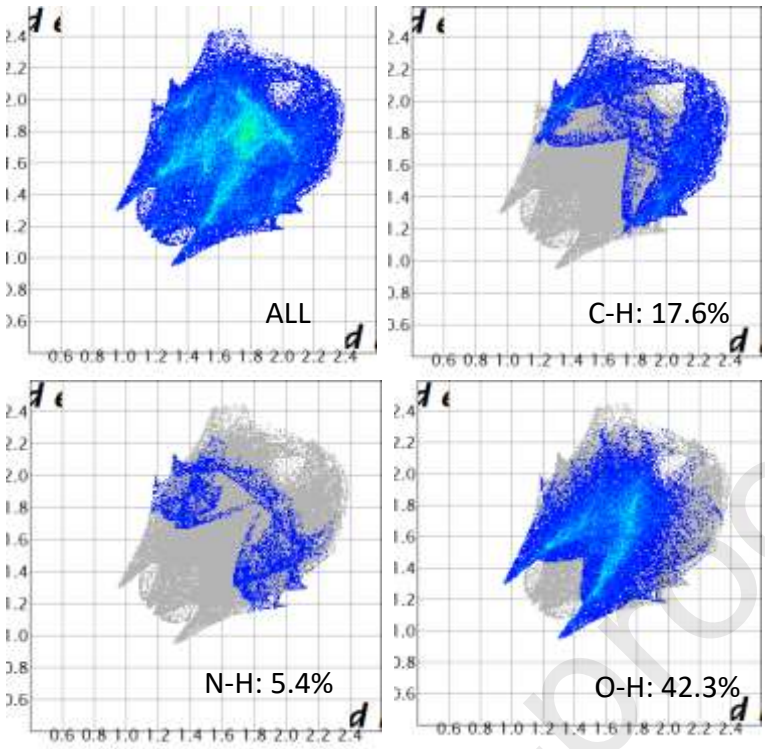

Figure 7. Fingerprint plot of [Zn(nba)$_2$(tmdp)]n **(1)** full and resolved into (B) H···O (C) H···H, and (D) H···C contacts showing the percentages of contacts contributed to the total Hirshfeld surface area.

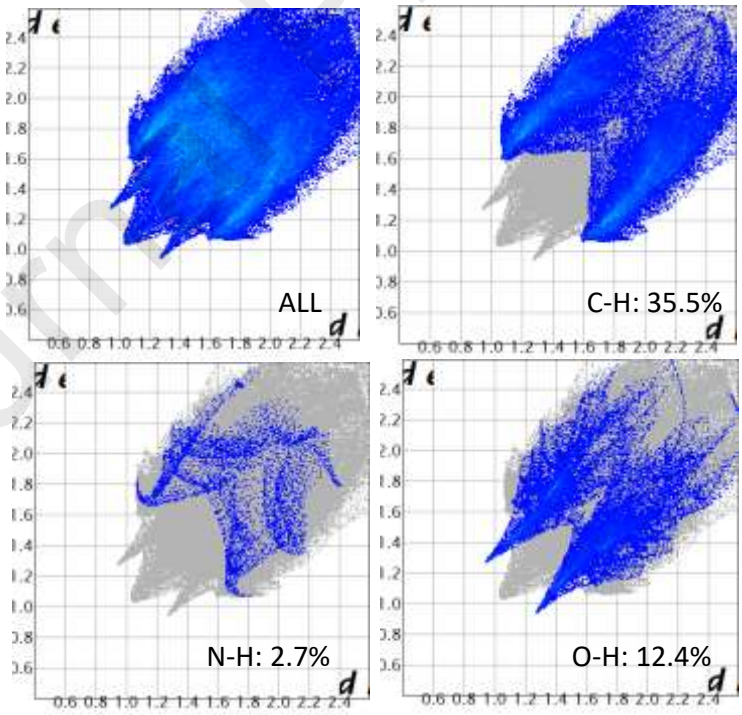

Figure 8: Fingerprint plot of [Zn(biphen)$_2$(tmdp)]n **(2)** full and resolved into (B) H···O (C) H···H, and (D) H···C contacts showing the percentages of contacts contributed to the total Hirshfeld surface area.

Table 2. Percentage contributions of selected interatomic contacts to the Hirschfeld surface of compounds.

	Surface interactions			
	C-H (%)	O-H (%)	N-H (%)	C-C (%)
[Zn(nba)$_2$(tmdp)]n (1)	17.6	42.3	5.4	2.9
[Zn(biphen)$_2$(tmdp)]n (2)	35.5	12.4	2.7	2.6

3.6 TGA/DSC

Thermogravimetric analysis was carried out for compounds **1** and **2** and the results are shown in **Figure S11**. Thermogram of **1** reveals a small weight loss around 100-120 °C which corresponds to 8% (calc.7.7%) of its weight, this accounts for the loss of the nitro group of one Hnba. The second weight loss of 47% (calc. 47.98%) between 240-400 °C corresponds to the thermal degradation of Hnba ligands of **1**. These two weight loss show endothermic peaks on the DSC curve at 252 and 298 °C, respectively. A further weight loss of about 32% (calc. 33.38%) was reported between 500-545 °C and it is attributed to the loss of tmdp ligand. The loss of tmdp resulted in an exothermic peak at 520°C leaving zinc oxide (observed 13%, calculated 13.59%) which is stable up to 800 °C.

For **2**, the TGA/DSC profile shows a thermally stable compound up to 260 °C. After which, mass loss of 87% (calc. 87.66%) occured between 260 °C to 500 °C *via* an unidentified step for the loss of two biphen and one tmdp ligands, to give the expected zinc oxide (observed 112.60%, calculated 12.33%) which remained stable up to 800^{o}C. The major exothermic peak was observed around 500^{o}C.

3.7 Adsorption studies

3.7.1 Initial comparison of MO removal in 1 and 2

The MO removal capacities of **1** and **2** were compared by investigating the adsorption of MO dye from aqueous medium with starting adsorbate concentration of 100 mg/L. It can be observed in Figure 9 that **1** exhibited better adsorption capacity towards MO than **2**, with the percentage adsorbed being 92.4% and 6.8% for **1** and **2** respectively, after stirring for 300 min. The adsorption capacities of **1** and **2** was 98.00 mg/g and 22.67 mg/g, respectively.

The results clearly revealed that **1** is more effective for the removal of MO compared to **2** and this is probably due to the high surface area and pore diameter it offers. Compound **2** was

excluded from further adsorption studies, due to the observed low preliminary sorption capacity.

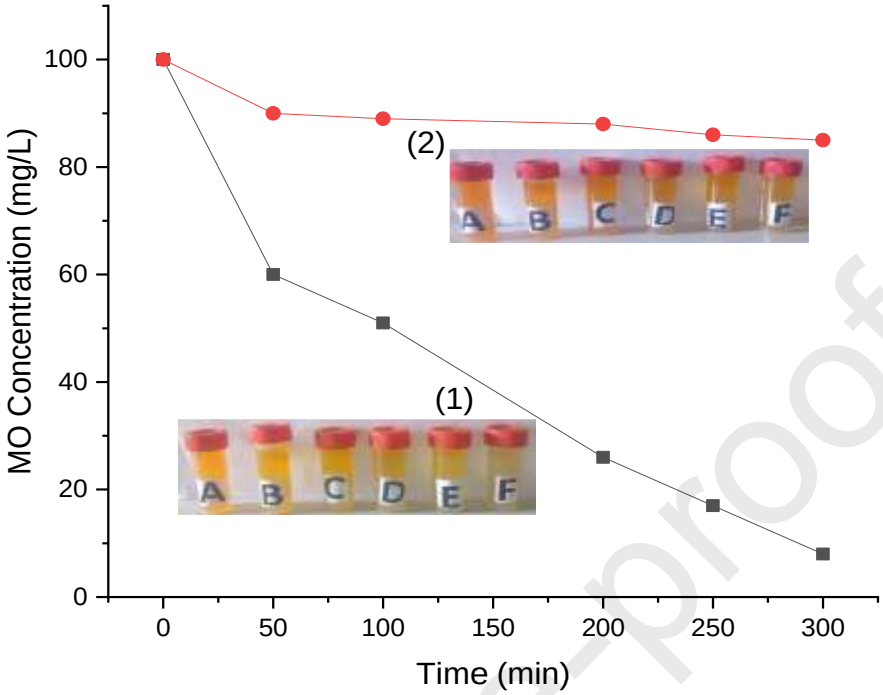

Figure 9: Time evolution of the MO concentration during its adsorption on **1** and **2.** (Inset: samples withdrawn at A: 0 min; B:50 min; C: 100 min; D: 200 min; E: 250 min; F: 300 min)

Since **1** exhibited an excellent uptake of MO dye, further studies on the adsorption process was carried out, some operational parameters (pH, adsorbent dosage, temperature, adsorbate initial concentration and contact time) were optimized, adsorption kinetics, isotherm and thermodynamics were also studied and reported.

3.7.2 Effect of pH

The pH_{PZC} of **1** (as shown in **Figure S12a**) was found to be 7.1 while the pKa of MO is 3.47. This implied that at pH less than 7.1, the charge on MO was positive, and at a pH greater than 7.1, the charge was negative. Adsorption was higher in the acidic range (<7) compared to the basic range (>7) (**Figure S12b**). Below pH 7, adsorption capacity was ~159.2 mg/g, increasing the pH from 7 to 12 resulted in a decrease in adsorption capacity from 159.2 mg/g to 24.59 mg/g. Under basic conditions, the charge on the adsorbent was negative, causing electrostatic repulsion between the negatively-charged MO dye and the adsorbent. Therefore, electrostatic interaction may have also enhanced the adsorption process [56].

3.7.3 Effect of adsorbent dosage

Various amounts of **1** (0.01 to 0.05 g) were added to 50 mL solution containing 200 mg/L MO to determine the maximum uptake. From **Figure S13**, the adsorbent dosage with the maximum adsorption capacity is 0.03 g. Therefore, 0.03 g adsorbent dosage was taken as the optimum.

3.7.4 Effect of temperature

The optimal temperature for the adsorption of MO on **1** was investigated (**Figure S14a**). The experiments were performed in the range 298 – 333 K. Adsorption capacity for MO by **1** was obtained at 298 K and adsorption decreased with an increase in temperature, indicating an exothermic adsorption process. The Van't Hoff plot for the adsorption process shows the calculated values of Δ*H,* Δ*S* and Δ*G* for the adsorption process **(Figure S14b** and **Table 3)**

Table 3: Thermodynamic parameters.

Temp (K)	ΔG ($kJmol^{-1}$)	ΔH ($kJ\ mol^{-1}$)	ΔS ($J\ mol^{-1}\ K^{-1}$)
298	-6.26	-22.35	-54.77
313	-5.45		
323	-4.91		
333	-4.37		

When the value of ΔH is less than 40 kJ mol^{-1}, the adsorption process is physisorption [57]. The calculated value of ΔH indicates physisorption process. The ΔG value is less than zero indicating that the process is spontaneous and feasible. The negative Δ*S* value indicates a high degree of order [58].

3.7.5 Effect of initial adsorbate concentration and adsorption isotherm

Optimization studies for the adsorption capacity of the adsorbent was done by introducing 0.03 g of compound **1** to 50 mL of different concentrations of the adsorbate solution (20-500 mg/L) at 298 K and respective optimum pH values for 120 min. The uptake of MO by **1** increased from 13 to 549 mg/g when the concentration was raised from 20 to 500 mg/L (**Figure S15)**. Maximum adsorption is achieved when the easily accessible large vacant cavities are saturated [59].

The data was fitted into Langmuir, Freundlich, Temkin and Dubinin-Radushkevich (D-R) models as shown in **Figures S16a-d**. The equations are shown in **Table S2**. From the R^2 values, Freundlich model fitted best, indicating multilayer sorption on the adsorbent. The mean sorption energy, E, obtained from the adsorption of MO on **1** is 0.11, indicating a physisorption process [60]. The isotherm parameters and correlation coefficient values are presented in **Table 4.**

Table 4: Isotherm parameters.

Isotherm model	**Parameter**	**Values**
Langmuir	Qm (mg/g)	-361
	K_L (L/mg)	-3.41E-3
	R^2	0.6702
Freundlich	N	0.77
	K_f	0.55
	R^2	0.9903
Temkin	B_I	173.45
	b_T (J/mol)	14.28
	K_T (L/mg)	0.057
	R^2	0.7207
Dubinin-Radushkevich	B_D (mol^2/J^2)	3.87E-5
	q_s (mg /g)	89.03
	E (kJ /mol)	0.11
	R^2	0.5983

3.7.6 Optimizing the amount of time required for adsorption

The influence of contact time on the adsorptive uptake of MO by **1**, is presented in **Figure S17**. This was studied by introducing 0.03 g of compound **1** to 50 mL of 500 mg/L MO dye solution at 298 K and respective optimum pH values for a time range of 30-480 min. The adsorption curves show fast adsorption in the first 300 min. After that, no obvious variation in adsorption was observed. This is due to the abundant adsorption sites quickly getting occupied at the start of the adsorption process leaving less sites which are difficult to occupy [21].

The kinetics data was fitted into pseudo-first-order (PFO) and pseudo-second-order (PSO) models. The equations and plot parameters are presented in **Table S3**. The adsorption kinetics plots are shown in **Figures S18a** and **S18b**. Since the R^2 value for PSO is higher than PFO model and the experimental adsorption capacity is closer to the calculated adsorption capacity from the PSO model than that of the pseudo first order, it can be said that the adsorption follows the PSO rate model.

The kinetics data was also analyzed by Intraparticle, Bangham and Boyd diffusion models to study the mass transfer mechanism. The relevant parameters of these models are also given in **Table 5**. **Figures S18c-**e show the results from these models. For the intraparticle diffusion model plot given in **Figure S18c**, the straight line obtained is non-zero and multilinear. This indicates that intraparticle diffusion is not the only rate-limiting step [61]. The first portion of the plot stands for boundary layer effect, the second represents intraparticle or pore diffusion while the third represents adsorption into the pores. The parameter, K_{id} is calculated from the slope of the second linear portion of the plot. The Bangham diffusion model was also used to verify the proposition that not only one reaction mechanism was involved in the adsorption process. The plot of the Bangham diffusion model (**Figure S18d**) also suggests that boundary layer diffusion was involved in adsorption but was not the only rate controlling step due to the multilinearity of the curves [62]. To know the process controlling the overall sorption rate (rate- determining step) the Boyd model plot was applied. If the Boyd plot is a straight line and passes through the origin, particle diffusion is said to be the rate limiting step, otherwise external mass transfer is the rate limiting step. As seen from **Figure S18e**, the linear plot is non-zero, indicating a film-diffusion controlled process [63].

Table 5: Kinetics parameters

Kinetic model	**Parameter**	**Values**
	qe exp (mg/g)	546.31
Pseudo-first order	K_1 (min^{-1})	0.018
	Qe (mg/g)	1420
	R^2	0.9280
Pseudo-second order	K_2 (mg/gmin)	1.75E-5
	Qe (mg/g)	544.20
	R^2	0.9873
Intraparticle diffusion	C(mg/g)	59.24

	Kp (mg/gmin$^{1/2}$)	26.72
	R^2	0.9865
Bangham	A	0.717
	K_0(g)	0.522
	R^2	0.9795
Boyd	B (sec^{-1})	0.012
	R^2	0.9553

3.7.7 Regeneration of used adsorbents

Reusability of used adsorbents is a very important factor to consider for commercial applications. The solvent desorption technique using ethanol was applied for the regeneration of spent **1**. The spent adsorbents were separated from the solutions, washed with deionized water and dried at 80ºC. The dry spent adsorbents were then added into 50 mL of 95% volume ethanol and shaken for 1 hr at RT. The desorbed adsorbate concentrations, C_{des} (mg/L) were quantified using the UV–Vis spectrophotometer at the λ_{max} of the adsorbate as done for the adsorption procedure. The percentage desorption was calculated from the equation:

Desorption (%) = $C_{des}/C_{ad} \times 100$……..**Equation 3.1**

Where C_{ad} = amount of adsorbate initially adsorbed and C_{des} = final concentration of the adsorbate in the desorption medium.

The adsorption-desorption cycle was done three times, and at the end of the second cycle there was a small decrease in the adsorption capacities of **1** (**Figure 10** and **Table S4**). MO percent adsorption on **1** had decreased by 5.05% after the third use.

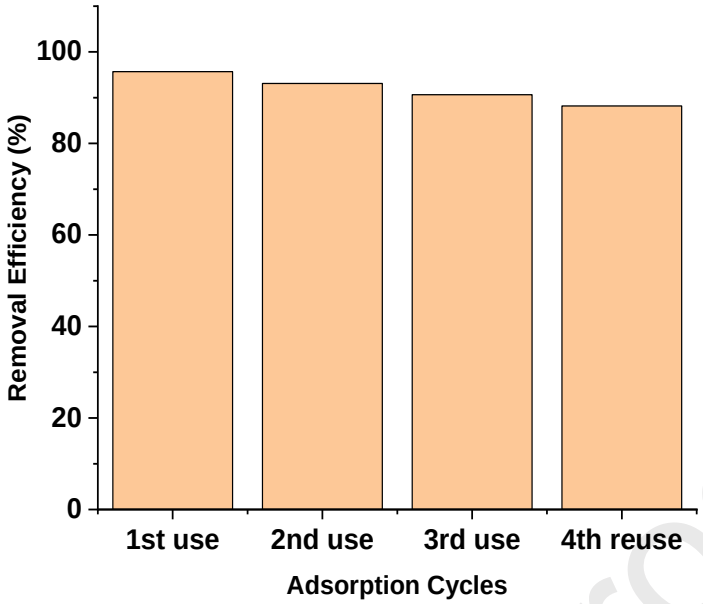

Figure 10: Adsorption cycles of **1** for MO adsorption.

PXRD measurements were performed to ascertain that crystallinity of **1** was maintained after the adsorption process. The PXRD spectrum in **Figure S19** indicates that there were no shifts or broadening of the peaks indicating that crystallinity was maintained. The FT-IR spectra of **1** and **1**-MO in the range 4000–400 cm^{-1} are shown in **Figure S20**. New peaks were assigned to some functional groups of MO while there were shifts of some other existing peaks. The shift of the asymmetric and symmetric COO^- bands at 1651 cm^{-1} and 1338 cm^{-1} to 1617 cm^{-1} and 1364 cm^{-1} respectively was observed. New band around 1900 cm^{-1} - 2000 cm^{-1} (in oval shape) ascribed to C=C asymmetric stretch of MO was seen in **1**-MO. The band around 1226 cm^{-1} on **1**-MO can be attributed to the sulfonate S=O bonds from MO, indicating the attachment of MO onto the surface of **1** [34].

3.8 Theoretical studies

Following successful adsorption studies (**Section 3.7**), theoretical studies were applied to determine the binding energies as well as the electronic interactions leading to the adsorption of MO on **1** and **2** using Biovia Materials Studio 2018. Biovia Forcite, an advanced classical molecular mechanics tool which allows fast geometry optimization and energy calculations was used for pre-optimization of structures. After calculating total energies of several possible starting positions in the interaction of the adsorbent and adsorbate, it was noted that

clusters where the adsorbate is positioned strategically to maximize pi-pi interactions with the groups in the adsorbent had the lowest total energies (**Figure 11**), meaning they are stable. Pi-pi interactions played a major role in determining the clusters with lowest energy. Where it was clear the adsorbent-adsorbate pi-pi interactions were well defined, the clusters had the lowest total energy. It was difficult to determine whether the Zn centre is directly involved in the physical interactions from the positions preferred by MO on **1** and **2** during Forcite pre-optimization.

Geometry optimization was then carried out using slightly modified literature methods in the Biovia DMol^3 module (**Figure 11** and **Table 5**) [42,43]. MO remains flat allowing its phenyl groups to interact with the phenyl groups in compounds **1** and **2**. In compound **1** MO lies parallel to the nitrobenzoic acid groups allowing each of its phenyl groups to interact with the adjacent nitrobenzoic groups. With compound **2**, the most stable complex is where MO is sandwiched between biphen and tmdp allowing the sulfonate end to interact with the carboxylic end phenyl of biphen while the amine phenyl end interacted with the tmdp phenyl. The interaction is less stable compared to the compound **1**-MO complex. The chance of such an interaction to occur in the polymeric form of compound **2** is also less likely due to steric hindrance. Considering that the binding energy between compound **2** and MO is lower compared to that between compound **1** and MO and the unlikelihood of the preferred position to occur in the bulk material, the lower adsorption capacity observed in **Section 3.7.1** is expected. The negative binding energies confirmed the feasibility of interaction. Adducts formed between **1** and MO indicated that HOMO (highest occupied molecular orbital) is centered on MO, while LUMO (lowest unoccupied molecular orbital) originated around 4-nitrobenzoic (Hnba) moiety (**Figure S21**). This clearly indicated that the interaction between the MO and **1** is mainly driven by electron donation from the HOMO to the LUMO.

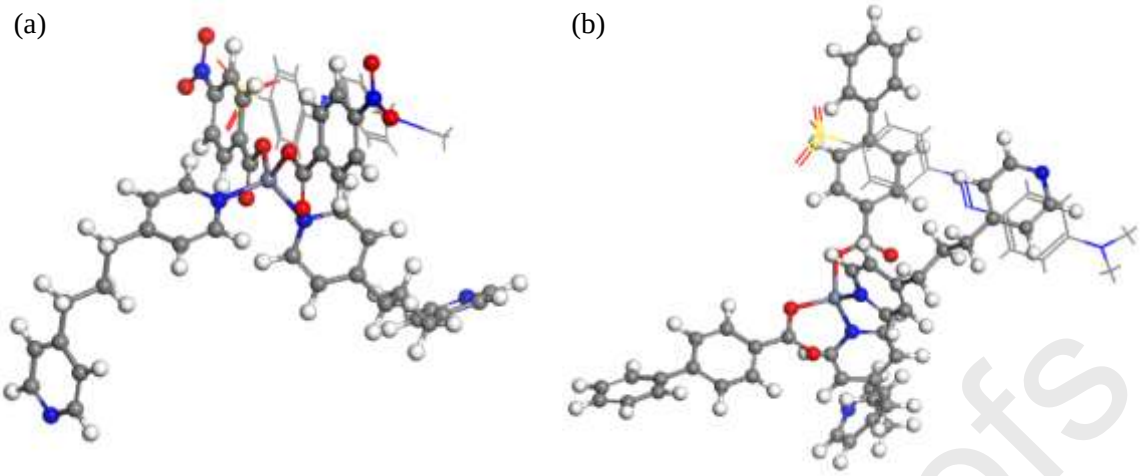

Figure 11. Biovia Materials Studio 2018 DMol^3 modelled structures showing adsorption of MO on **1** (a) neutral model and (b) anionic model.

Table 5. Energies of the adsorbents, adsorbates and their clusters; and calculations for binding energy (BE).

	$E_{\text{adsorbent + adsorbate}}$ (kJmol^{-1})	$E_{\text{adsorbent}}$ (kJmol^{-1})	$E_{\text{adsorbate}}$ (kJmol^{-1})	ΔE (kJmol^{-1})
1	-14657161.26	-11167559.84	-3489527.28	-74.14
2	-14795943.39	-11306355.00	-3489527.28	-61.11

ΔE (BE) = $E_{\text{adsorbent + adsorbate}} - (E_{\text{adsorbent}} + E_{\text{adsorbate}})$

3.9 Comparing adsorption of MO on 1 with other reported adsorbents

The adsorption capacity of **1** is relatively greater than that of most reported adsorbents as shown on **Table 6**. Coupled with its reusability which is favourable, this makes it an economical adsorbent for MO removal from wastewater.

Table 6: Performance evaluation of **1** in MO removal compared to other literature materials.

Adsorbent	**Qm (mg/g)**	**Reference**
Mesoporous carbon	294.1	[19]
Functionalized chromium-benzenedicarboxylates MOF	194-241	[56]
Anion–cationic surfactants modified montmorillonite	54	[64]
EDTA-functionalized electrospun	99.15	[58]

polyacrylonitrile nanofibers		
Cd-based metal-organic framework	166	[34]
Compound **1**	546.31	This work

3.10 Conclusions

The synthesis of coordination polymers; $[Zn(nba)_2(tmdp)]_n$ (**1**) and $[Zn(biphen)_2(tmdp)]_n$ (**2**) and the removal efficiency of MO dye by (**1**) was reported. The adsorption capacity of **1** towards MO was found to be 546.31 mg/g and higher than **2** (22.67 mg/g). Freundlich isotherm and pseudo second order kinetic models were found to fit best. Hirshfeld surface analyses indicated that compound (**1**) contributed a higher O–H···O interaction compared to (**2**), while, DFT studies showed that pi-pi interactions also played a crucial role in the adsorption of MO. It was also demonstrated that the adsorbent can be regenerated and reused even after four adsorption cycles with minimal loss of adsorption capacity. The results of the adsorption process demonstrated that **1** could serve as effective candidate adsorbent for the removal of methyl orange from wastewater.

Supplementary data

CCDC **1954756** and **1954762** contains the crystallographic data of $[Zn(nba)_2(tmdp)]_n$ (**1**) and $[Zn(biphen)_2(tmdp)]_n$ (**2**), respectively. The data can be obtained free of charge from the Cambridge Crystallographic Data Centre via www.ccdc.cam.ac.uk/structures.

Conflict of Interest

The authors declare no conflict of interests.

Acknowledgement

A.C. Oladipo is grateful to the Royal Society of Chemistry for the Researchers' Mobility Grant award, and the University of Warwick's Research Technology Platforms, for the provision of facilities for the analysis of the compounds. The authors thank the Centre for High Performance Computing (CHPC), Cape Town, South Africa for providing the platform for DFT studies using Biovia Materials Studio 2018.

References

[1] K. Biradha, A. Ramanan, J.J. Vittal, Coordination polymers versus metal-organic frameworks, Cryst. Growth Des. 9 (2009) 2969–2970. https://doi.org/10.1021/cg801381p.

[2] S. Ma, H.C. Zhou, Gas storage in porous metal-organic frameworks for clean energy applications, Chem. Commun. 46 (2010) 44–53. https://doi.org/10.1039/b916295j.

[3] L. Ma, W. Lin, Designing Metal-Organic Frameworks for Catalytic Applications, Top. Curr. Chem. 293 (2010) 175–205.

[4] M.D. Allendorf, C.A. Bauer, R.K. Bhakta, R.J.T. Houk, Luminescent metal-organic frameworks, Chem. Soc. Rev. 38 (2009) 1330–1352. https://doi.org/10.1039/b802352m.

[5] A.C. McKinlay, R.E. Morris, P. Horcajada, G. Férey, R. Gref, P. Couvreur, C. Serre, BioMOFs: Metal-organic frameworks for biological and medical applications, Angew. Chemie - Int. Ed. 49 (2010) 6260–6266. https://doi.org/10.1002/anie.201000048.

[6] B.I. Kharisov, P.E. Martínez, V.M. Jiménez-Pérez, O. V. Kharissova, B.N. Martínez, N. Pérez, Recent advances on ditopic ligands, J. Coord. Chem. 63 (2010) 1–25. https://doi.org/10.1080/00958970903325534.

[7] Z. Liu, Y.M. Ng, P.J. Tiong, R. Asyikin, A. Talip, N. Jasin, V. Yi, M. Jong, M.G. Tay, Five-Coordinate Zinc (II) Complex : Synthesis , Characterization , Molecular Structure , and Antibacterial Activities of Bis- [(E) -2- hydroxy- N □ - { 1- (4- methoxyphenyl) ethylidene } benzohydrazido] dimethylsulfoxidezinc (II) Complex, 2017 (2017).

[8] A.M. Awad, S.M.R. Shaikh, R. Jalab, M.H. Gulied, M.S. Nasser, A. Benamor, S. Adham, Adsorption of organic pollutants by natural and modified clays: A comprehensive review, Sep. Purif. Technol. 228 (2019). https://doi.org/10.1016/j.seppur.2019.115719.

[9] A.H. Alabi, A.I. Buhari-Alade, F.O. Sholaru, R.F. Awoyemi, Biosorption of Phenols and Dyes on Albizia lebbeck (Rattle Seed) Pod: Equilibrium and Kinetic Studies, CRDEEP Journals Int. J. Environ. Sci. Alimoh H. Alabi et. Al. 5 (2015) 154–165. www.crdeepjournal.org/ijes.

[10] L. Bulgariu, L.B. Escudero, O.S. Bello, M. Iqbal, J. Nisar, K.A. Adegoke, F. Alakhras, M. Kornaros, I. Anastopoulos, The utilization of leaf-based adsorbents for dyes removal: A review, J. Mol. Liq. 276 (2019) 728–747. https://doi.org/10.1016/j.molliq.2018.12.001.

[11] A.P. Aziztyana, S. Wardhani, Y.P. Pranato, D.Purwonugroho, A. Darjito, Optimisation of Methyl Orange Photodegradation using TiO_2 - Zeolite Photocatalyst and H_2O_2 in Acid Condition, IOP Conf. Ser. Mater. Sci. Eng, 546 (2019), 042047. doi: 10.1088/1757-899X/546/4/ 042047.

[12] V.K.Meena, and R.C. Meena, Studies on Photodegradation of Methyl orange in aqueous solution using immobilized dowex-11 Photocatalyst , J. Ind. Council Chem. 27 , (2010) 2, 180-184

[13] J.J. Du, Y.P. Yuan, J.X. Sun, F.M. Peng, X. Jiang, L.G. Qiu, A.J. Xie, Y.H. Shen, J.F. Zhu, New photocatalysts based on MIL-53 metal-organic frameworks for the decolorization of methylene blue dye, J. Hazard. Mater. 190 (2011) 945–951. https://doi.org/10.1016/j.jhazmat.2011.04.029.

[14] K. Murugesan, Y.M. Kim, J.R. Jeon, Y.S. Chang, Effect of metal ions on reactive dye decolorization by laccase from Ganoderma lucidum, J. Hazard. Mater. 168 (2009) 523–529. https://doi.org/10.1016/j.jhazmat.2009.02.075.

[15] N. Nikooe, E. Saljoughi, Preparation and characterization of novel PVDF nanofiltration membranes with hydrophilic property for filtration of dye aqueous solution, Appl. Surf. Sci. 413 (2017) 41–49. https://doi.org/10.1016/j.apsusc.2017.04.029.

[16] A. Kumar Paul, G. Madras, S. Natarajan, Adsorption-desorption and photocatalytic properties of inorganic-organic hybrid cadmium thiosulfate compounds, Phys. Chem. Chem. Phys. 11 (2009) 11285–11296. https://doi.org/10.1039/b913407g.

[17] V. Singh, A.K. Sharma, S. Maurya, Efficient cadmium(II) removal from aqueous solution using microwave synthesized guar gum-graft-poly(ethylacrylate), Ind. Eng. Chem. Res. 48 (2009) 4688–4696. https://doi.org/10.1021/ie801416z.

[18] B. Van De Voorde, B. Bueken, J. Denayer, D. De Vos, Adsorptive separation on metal-organic frameworks in the liquid phase, Chem. Soc. Rev. 43 (2014) 5766–5788. https://doi.org/10.1039/c4cs00006d.

[19] N. Mohammadi, H. Khani, V.K. Gupta, E. Amereh, S. Agarwal, Adsorption process of methyl orange dye onto mesoporous carbon material-kinetic and thermodynamic studies, J. Colloid Interface Sci. 362 (2011) 457–462. https://doi.org/10.1016/j.jcis.2011.06.067.

[20] Y. Haldorai, J.J. Shim, An efficient removal of methyl orange dye from aqueous

solution by adsorption onto chitosan/MgO composite: A novel reusable adsorbent, Appl. Surf. Sci. 292 (2014) 447–453. https://doi.org/10.1016/j.apsusc.2013.11.158.

[21] Z. Luo, M. Gao, Y. Ye, S. Yang, Modification of reduced-charge montmorillonites by a series of Gemini surfactants: Characterization and application in methyl orange removal, Appl. Surf. Sci. 324 (2015) 807–816. https://doi.org/10.1016/j.apsusc.2014.11.043.

[22] J.R. Li, J. Sculley, H.C. Zhou, Metal-organic frameworks for separations, Chem. Rev. 112 (2012) 869–932. https://doi.org/10.1021/cr200190s.

[23] P. Silva, S.M.F. Vilela, J.P.C. Tomé, F.A. Almeida Paz, Multifunctional metal-organic frameworks: From academia to industrial applications, Chem. Soc. Rev. 44 (2015) 6774–6803. https://doi.org/10.1039/c5cs00307e.

[24] (24) Z. Zhang, Z.Z. Yao, S. Xiang, B. Chen, Perspective of microporous metal-organic frameworks for CO2 capture and separation, Energy Environ. Sci. 7 (2014) 2868–2899. https://doi.org/10.1039/c4ee00143e.

[25] Z. Hasan, S.H. Jhung, Removal of hazardous organics from water using metal-organic frameworks (MOFs): Plausible mechanisms for selective adsorptions, J. Hazard. Mater. 283 (2015) 329–339. https://doi.org/10.1016/j.jhazmat.2014.09.046.

[26] I. Ahmed, S.H. Jhung, Applications of metal-organic frameworks in adsorption/separation processes via hydrogen bonding interactions, Chem. Eng. J. 310 (2017) 197–215. https://doi.org/10.1016/j.cej.2016.10.115.

[27] E. Haque, J.W. Jun, S.H. Jhung, Adsorptive removal of methyl orange and methylene blue from aqueous solution with a metal-organic framework material, iron terephthalate (MOF-235), J. Hazard. Mater. 185 (2011) 507–511. https://doi.org/10.1016/j.jhazmat.2010.09.035.

[28] S.H. Huo, X.P. Yan, Metal-organic framework MIL-100(Fe) for the adsorption of malachite green from aqueous solution, J. Mater. Chem. 22 (2012) 7449–7455. https://doi.org/10.1039/c2jm16513a.

[29] P.Y. Du, H. Li, X. Fu, W. Gu, X. Liu, A 1D anionic lanthanide coordination polymer as an adsorbent material for the selective uptake of cationic dyes from aqueous solutions, Dalt. Trans. 44 (2015) 13752–13759. https://doi.org/10.1039/c5dt01848j.

[30] G.I. Dzhardimalieva, R.K. Baimuratova, E.I. Knerelman, G.I. Davydova, S.E. Kudaibergenov, O. V. Kharissova, V.A. Zhinzhilo, I.E. Uflyand, Synthesis of copper(II) trimesinate coordination polymer and its use as a sorbent for organic dyes and a precursor for nanostructured material, Polymers (Basel). 12 (2020) 1024.

https://doi.org/10.3390/POLYM12051024.

[31] C. Liang, J. Ren, S. El Hankari, J. Huo, Aqueous Synthesis of a Mesoporous Zr-Based Coordination Polymer for Removal of Organic Dyes, ACS Omega. 5 (2020) 603–609. https://doi.org/10.1021/acsomega.9b03192.

[32] W.Y. Yin, T.T. Bian, J. Geng, Y.H. Hu, S.Q. Yan, X.Y. Tang, H.J. Cheng, Y.S. Ma, R.X. Yuan, Synthesis, structure and adsorption studies of a nickel coordination polymer with selective removal on methyl orange, Inorganica Chim. Acta. 476 (2018) 1–6. https://doi.org/10.1016/j.ica.2018.01.025.

[33] A.C. Tella, S.O. Owalude, C.A. Ojekanmi, O.S. Oluwafemi, Synthesis of copper-isonicotinate metal-organic frameworks simply by mixing solid reactants and investigation of their adsorptive properties for the removal of the fluorescein dye, New J. Chem. 38 (2014) 4494–4500. https://doi.org/10.1039/c4nj00411f.

[34] A.C. Tella, M.D. Olawale, M. Neuburger, J.A. Obaleye, Synthesis and crystal structure of Cd-based metal-organic framework for removal of methyl-orange from aqueous solution, J. Solid State Chem. 255 (2017) 157–166. https://doi.org/10.1016/j.jssc.2017.07.019.

[35] A.C. Tella, M.D. Olawale, J.A. Obaleye, V.O. Adimula, L.O. Alimi, P.A. Ajibade, Removal of organic pollutant (pyrene) from aqueous solution using coordination polymer of [Cu(Pic)2(H2O)2]·H2O (CP-1) as adsorbent, Appl. Water Sci. 9 (2019) 159. https://doi.org/10.1007/s13201-019-1039-0.

[36] M.D. Olawale, A.C. Tella, J.A. Obaleye, J.S. Olatunji, Synthesis, characterization and crystal structure of a copper-glutamate metal organic framework (MOF) and its adsorptive removal of ciprofloxacin drug from aqueous solution, New J. Chem. 44 (2020) 3961–3969. https://doi.org/10.1039/d0nj00515k.

[37] A.C. Tella, S.O. Owalude, S.J. Olatunji, S.O. Oloyede, A.S. Ogunlaja, S.A. Bourne, Synthesis, crystal structure and desulfurization properties of zig-zag 1D coordination polymer of copper(II) containing 4-methoxybenzoic acid ligand, J. Sulfur Chem. 39 (2018) 588–606. https://doi.org/10.1080/17415993.2018.1489808.

[38] A.C. Tella, A.C. Oladipo, V.O. Adimula, O.A. Ameen, S.A. Bourne, A.S. Ogunlaja, Synthesis and crystal structures of a copper(II) dinuclear complex and zinc(ii) coordination polymers as materials for efficient oxidative desulfurization of dibenzothiophene, New J. Chem. 43 (2019) 14343–14354. https://doi.org/10.1039/c9nj01456j.

[39] O. V. Dolomanov, L.J. Bourhis, R.J. Gildea, J.A.K. Howard, H. Puschmann, OLEX2:

A complete structure solution, refinement and analysis program, J. Appl. Crystallogr. 42 (2009) 339–341. https://doi.org/10.1107/S0021889808042726.

[40] G.M. Sheldrick, SHELXT - Integrated space-group and crystal-structure determination, Acta Crystallogr. Sect. A Struct. Chem. A71 (2015) 3–8.

[41] G.M. Sheldrick, Crystal structure refinement with SHELXL, Acta Crystallogr. Sect. C Struct. Chem. 71 (2015) 3–8. https://doi.org/10.1107/S2053229614024218.

[42] I. Ahmed, M. Tong, J.W. Jun, C. Zhong, S.H. Jhung, Adsorption of Nitrogen-Containing Compounds from Model Fuel over Sulfonated Metal-Organic Framework: Contribution of Hydrogen-Bonding and Acid-Base Interactions in Adsorption, J. Phys. Chem. C. 120 (2016) 407–415. https://doi.org/10.1021/acs.jpcc.5b10578.

[43] Z. Chen, L. Ling, B. Wang, H. Fan, J. Shangguan, J. Mi, Adsorptive desulfurization with metal-organic frameworks: A density functional theory investigation, Appl. Surf. Sci. 387 (2016) 483–490. https://doi.org/10.1016/j.apsusc.2016.06.078.

[44] G.B. Deacon, R.J. Phillips, Relationships between the carbon-oxygen stretching frequencies of carboxylato complexes and the type of carboxylate coordination, Coord. Chem. Rev. 33 (1980) 227–250. https://doi.org/10.1016/S0010-8545(00)80455-5.

[45] M.A. Wani, A. Kumar, M.D. Pandey, R. Pandey, Heteroleptic 1D coordination polymers: 5-Coordinated zinc(II) polymer as an efficient transesterification catalyst, Polyhedron. 126 (2017) 142–149. https://doi.org/10.1016/j.poly.2017.01.027.

[46] L.Y. Xin, Y.P. Li, F.Y. Ju, X.L. Li, G.Z. Liu, A supramolecular microporous network of zinc(II) coordination polymer for highly selective fluorescent detection of Pb2+, Indian J. Chem. - Sect. A Inorganic, Phys. Theor. Anal. Chem. 56A (2017) 826–831.

[47] A. Okuniewski, D. Rosiak, J. Chojnacki, B. Becker, Coordination polymers and molecular structures among complexes of mercury(II) halides with selected 1-benzoylthioureas, Polyhedron. 90 (2015) 47–57. https://doi.org/10.1016/j.poly.2015.01.035.

[48] L. Yang, D.R. Powell, R.P. Houser, Structural variation in copper(i) complexes with pyridylmethylamide ligands: Structural analysis with a new four-coordinate geometry index, τ4, J. Chem. Soc. Dalt. Trans. 955 (2007) 955–964. https://doi.org/10.1039/b617136b.

[49] C. Liu, Z. Chen, X. Li, J. Tang, A concise synthesis of tetrabenazine and its crystal structure, Mol. Cryst. Liq. Cryst. 557 (2012) 39–49. https://doi.org/10.1080/15421406.2011.627764.

[50] P. Mahata, G. Madras, S. Natarajan, Novel photocatalysts for the decomposition of

organic dyes based on metal-organic framework compounds, J. Phys. Chem. B. 110 (2006) 13759–13768. https://doi.org/10.1021/jp0622381.

[51] F.A. Almeida Paz, J. Klinowski, Two- and three-dimensional cadmium-organic frameworks with trimesic acid and 4,4′-trimethylenedipyridine, Inorg. Chem. 43 (2004) 3882–3893. https://doi.org/10.1021/ic049523o.

[52] N.E. Clayman, M.A. Manumpil, D. Umeyama, A.E. Rudenko, H.I. Karunadasa, R.M. Waymouth, Carving Out Pores in Redox-Active One-Dimensional Coordination Polymers, Angew. Chemie - Int. Ed. 57 (2018) 14585–14588. https://doi.org/10.1002/anie.201807506.

[53] M. Sánchez-Serratos, J.R. Álvarez, E. González-Zamora, I.A. Ibarra, Porous coordination polymers (Pcps): New platforms for gas storage, J. Mex. Chem. Soc. 60 (2016) 43–57. https://doi.org/10.29356/jmcs.v60i2.72.

[54] W.L. Leong, J.J. Vittal, One-demensional coordination polymers: Complexity and diversity in structures, properties, and applications, Chem. Rev. 111 (2011) 688–764. https://doi.org/10.1021/cr100160e.

[55] M. J Turner, J.J.McKinnon, S.K.Wolff, D.J.Grimwood, P.R. Spackman, D. Jayatilaka, M.A.Spackman, CrystalExplorer17. **2017**, The University of Western Australia.

[56] E. Haque, J.E. Lee, I.T. Jang, Y.K. Hwang, J.S. Chang, J. Jegal, S.H. Jhung, Adsorptive removal of methyl orange from aqueous solution with metal-organic frameworks, porous chromium-benzenedicarboxylates, J. Hazard. Mater. 181 (2010) 535–542. https://doi.org/10.1016/j.jhazmat.2010.05.047.

[57] J. Fan, J. Zhang, C. Zhang, L. Ren, Q. Shi, Adsorption of 2,4,6-trichlorophenol from aqueous solution onto activated carbon derived from loosestrife, Desalination. 267 (2011) 139–146. https://doi.org/10.1016/j.desal.2010.09.016.

[58] R.M. Nthumbi, A.A. Adelodun, J.C. Ngila, Electrospun and functionalized PVDF/PAN composite for the removal of trace metals in contaminated water, Phys. Chem. Earth. 100 (2017) 225–235. https://doi.org/10.1016/j.pce.2016.08.007.

[59] P. Sejie, S. Nadiye-Tabbiruka, Removal of Methyl Orange (MO) from Water by adsorption onto Modified Local Clay (Kaolinite), Phys. Chem. 6 (2016) 39–48. https://doi.org/10.5923/j.pc.20160602.02.

[60] A.S. Özcan, B. Erdem, A. Özcan, Adsorption of Acid Blue 193 from aqueous solutions onto Na-bentonite and DTMA-bentonite, J. Colloid Interface Sci. 280 (2004) 44–54. https://doi.org/10.1016/j.jcis.2004.07.035.

[61] L. Cui, X. Guo, Q. Wei, Y. Wang, L. Gao, L. Yan, T. Yan, B. Du, Removal of

mercury and methylene blue from aqueous solution by xanthate functionalized magnetic graphene oxide: Sorption kinetic and uptake mechanism, J. Colloid Interface Sci. 439 (2015) 112–120. https://doi.org/10.1016/j.jcis.2014.10.019.

[62] A.A. Inyinbor, F.A. Adekola, G.A. Olatunji, Kinetics, isotherms and thermodynamic modeling of liquid phase adsorption of Rhodamine B dye onto Raphia hookerie fruit epicarp, Water Resour. Ind. 15 (2016) 14–27. https://doi.org/10.1016/j.wri.2016.06.001.

[63] S. Nethaji, A. Sivasamy, A.B. Mandal, Preparation and characterization of corn cob activated carbon coated with nano-sized magnetite particles for the removal of Cr(VI), Bioresour. Technol. 134 (2013) 94–100. https://doi.org/10.1016/j.biortech.2013.02.012.

[64] D. Chen, J. Chen, X. Luan, H. Ji, Z. Xia, Characterization of anion-cationic surfactants modified montmorillonite and its application for the removal of methyl orange, Chem. Eng. J. 171 (2011) 1150–1158. https://doi.org/10.1016/j.cej.2011.05.013.

Highlights

- Two novel zinc coordination polymers $[Zn(nba)_2(tmdp)]_n$ and $[Zn(biphen)_2(tmdp)]_n$ were synthesized by stirring in DMF at ambient temperature.
- They were investigated for the adsorptive removal of methyl orange (MO) dye from water.
- $[Zn(nba)_2(tmdp)]_n$ exhibited higher removal of MO (546.31 mg/g) than $[Zn(biphen)_2(tmdp)]_n$ (22.67 mg/g).
- DFT studies indicated that the adsorption was aided by π-π stacking and electrostatic interactions.

Graphical Abstract Synopsis

Two new zinc (II) coordination polymers, $[Zn(nba)_2(tmdp)]_n$ and $[Zn(biphen)_2(tmdp)]_n$, were synthesized and characterized using microanalysis, spectroscopic techniques and single x-ray crystallography. They were used for removal of methyl orange from aqueous solution, thereby positioning them as adsorbents for environmental remediation. Mechanism of adsorption was analyzed using DFT studies.

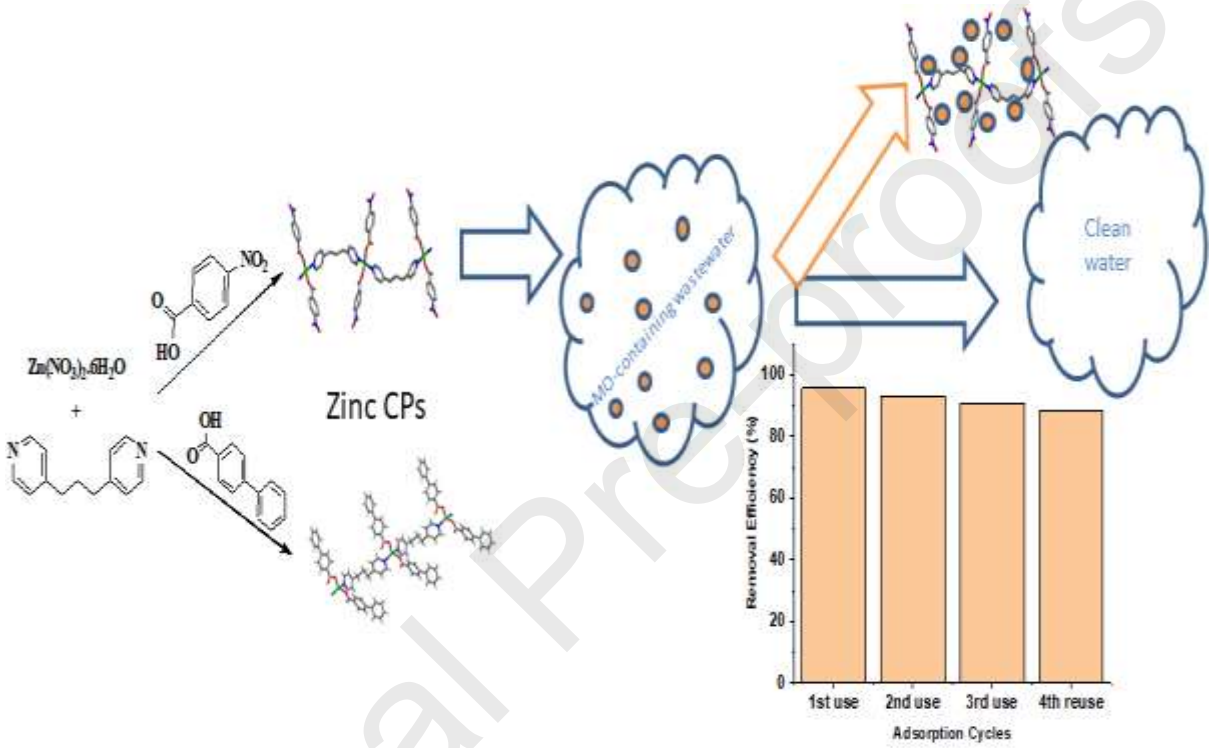

Credit Author Statement

A. C. Oladipo, V.T.Olayemi, V.O.Adimula - Conceptualization, Methodology, Data curation, Writing Original Draft.

A. C. Tella, R. I. Walton, A.S. Ogunlaja - Formal analysis,Supervision,Funding Acquisition , Writing and Editing.

A.S. Ogunlaja ,

T.O. Dembaremba , A .C. Tella DFT studies, Supervision, Review and Editing

Supervision, Writing and Editing.

G.Y.Clarkson and R.I. WaIton X-ray Structure analysis and Discussion